Seasonal and diurnal variations of vorticity and divergence in the Eastern Boundary Current Systems

Antonio Quintana[1], **Hector S. Torres**[2], **and Jose Gomez-Valdes**[1]

[1]Departamento de Oceanografía Física, Centro de Investigación Científica y de Educación Superior de Ensenada (CICESE), Ensenada, México
[2]Jet Propulsion Laboratory, California Institute of Technology, Pasadena, California

Key Points:

- We can isolate submesoscale features in low-energy current systems, such as Eastern Boundary Currents.
- There is a 2 to 3.5-hour delay between divergence and vorticity in the Eastern Boundary Currents in winter, with a latitudinal dependency.
- Atmospheric forcings and seasonality play an essential role in the modulation of submesoscales within the four major Eastern Boundary Currents.

Corresponding author: Antonio Quintana, cesarperez@cicese.edu.mx

Abstract

Eastern Boundary Currents Systems are typically studied as a whole due to their dynamical similarities, mainly because Ekman pumping is predominant at these currents, and they typically have low kinetic energy. In this study, we used the output of a high-resolution global simulation to make a dynamical comparison among the California, Canary, Peru, and Benguela currents during the winter and summer months, focusing on submesoscale motions ($Ro \sim 1$) in both the frequency-wavenumber and space-time domains. After we confirmed the presence of submesoscale activity and isolated it from mesoscale motions, we found that their divergence and vorticity fields follow similar seasonal patterns in the near-diurnal frequency range, despite regional differences. The results showed that heat fluxes at the ocean surface, along with weak to moderate wind stresses, significantly impact the modulation of submesoscale vorticity and divergence fields at diurnal frequencies.

Plain Language Summary

We used the output of a realistic, high-resolution global ocean simulation (LLC4320) to analyze the four major Eastern Boundary Currents: California, Canary, Peru, and Benguela. Our study is first focused on identifying and isolating submesoscale motions by calculating a scale (transition scale, L_t) so that all motions smaller than that scale belong to the *submesoscale regime*. Then we compare submesoscale divergence and vorticity across the four currents, demonstrating that they remain similar at smaller scales, even though there are noticeable differences among them. Finally, by looking at time series of the evolution of the intensity of local divergence and vorticity, we found a clear diurnal cycle and the presence of a latitude-dependent delay between these dynamical variables, whose explanation relies on the role played by atmospheric forcings, with this influence being stronger in winter than in summer.

1 Introduction

Eastern Boundary Currents (hereinafter EBC) have been of interest since, to a first approximation, they exhibit the same dynamical behavior; thus, current literature typically describes EBC as a single entity (Tomczak, 1981; Hill et al., 1998). Their similarities allow us to define them as current systems located on the eastern side of ocean basins within the subtropical oceanic gyres, where surface currents move equatorward along with the global wind patterns. Since wind runs alongshore in EBC, Ekman dynamics transport rich-nutrient water to the mixed layer (Chereskin & Price, 2008), feeding the base of the trophic chain, which therefore explains why a large portion of the world fishery takes places within these regions(Fréon et al., 2009). Also, low-frequency relaxation of alongshore winds creates an undercurrent that flows poleward, following the continental slope (Samelson, 2017).

Oceanic submesoscale currents play a crucial role in oceanic phenomena such as vertical transport of tracers and mass in the upper ocean (Thomas & Ferrari, 2008). These motions occur predominantly within the mixed layer, where secondary circulations arise from lateral density gradients induced by larger-scale flows. In contrast, mesoscale balanced motions (hereinafter BM) such as zonal jets and eddies usually extend below the mixed layer depth, a feature that allows us to distinguish submesoscale from mesoscale more intuitively. Even though they have different spatial and temporal scales, recent research has found evidence of interaction across these two physical regimes, thus altering energy budgets and mean transport in the sea (Müller et al., 2015; Thomas, 2017; Qiu et al., 2017; Klein et al., 2019).

Analyses of submesoscale phenomena require intensive measurements in both space $O(10\ km)$ and time $O(1\ h)$ to achieve submesoscale scales. This challenge increases when we attempt to study broader areas such as the four major EBC during a complete season. For instance, while future satellite missions will achieve spatial resolution, it will be at the expense of a low sampling frequency because a single or even a limited number of satellites cannot cover the entire ocean at the same time. Nevertheless, as computational power has grown in recent years,

high-resolution global simulations of the ocean with realistic atmospheric and tidal forcings are currently available, enabling us to study oceanic motions and the interaction across its different spatiotemporal scales. Furthermore, the increased temporal resolution allows us to research internal gravity waves (hereinafter IGW) and their impact on the energy budgets in EBC since internal waves account for a higher portion of the total kinetic energy in EBC (Torres et al., 2018), unlike Western Boundary Currents (e.g., the Gulf Stream or the Kuroshio current) where westward intensification generates intense geostrophic currents.

Here we present a study that characterises submesoscale relative vorticity (RV) and divergence (DIV) fields in $6°\times6°$ (~ 500 km side at mid-latitudes) regions within the four major EBC: California, Peru, Canary and Benguela currents (as displayed in Fig. 1). This research extends the results obtained by Qiu et al. (2018), Chereskin and Price (2008) and Torres et al. (2018), then applies them to the four EBC in both mesoscale and submesoscale regimes by comparing and highlighting their seasonal features. Although simulation data is available for the whole ocean, their Fourier spectra cannot be calculated for regions with land portions (i.e. islands and coasts); that explains the absence of study areas for some EBC or near the coastline, so we took as many as possible for our research.

We examined both the time-space (x, y, t) and frequency-wavenumber (ω, k_h) domains for the summer and winter months in 2012. Our starting point is the collection of $\omega - k_h$ spectra from Torres et al. (2018) for surface kinetic energy, along with its vortical and divergent parts, which we integrated for all frequencies and obtained their corresponding horizontal wavenumber (k_h) spectra, following previous work (Qiu et al., 2018; Torres et al., 2018). As for the spatiotemporal data, we employed the output of a realistic high-resolution ocean simulation (LLC4320) based on the Massachusetts Institute of Technology general circulation model (MITgcm). We took advantage of these high-resolution wavenumber spectra to find the horizontal scale such that submesoscale is more energetic for motions smaller than it; we call it the *transition scale*, L_t, as it displays a similar pattern to what Qiu et al. (2018) obtained. Then, we high-pass filtered submesoscale motions, with L_t as the horizontal cutoff scale. Moving forward, time series of submesoscale vorticity and divergence displays a phase difference at the diurnal component.

In the next two years, two experiments will collect in situ, airborne and satellite observations in the California Current System: S-MODE (Sub-Mesoscale Ocean Dynamics Experiment, `https://espo.nasa.gov/s-mode/content/S-MODE`) and the SWOT Cal/Val experiment (calibration and validation of the Surface and Water Ocean Topography mission) (Wang et al., 2019). The former experiment will test the hypothesis that submesoscale balanced motions (hereinafter SBM) make essential contributions to vertical exchanges of physical variables in the upper ocean. The latter will be dedicated to the calibration and validation of SWOT sea surface height (SSH) measurements at high spatial resolution (Wang et al., 2019). In anticipation of these experiments, the present study, based on numerical simulations, aims to further document the spatial and temporal characteristics of SBM and IGW in the EBC.

Our results show that most areas within EBC obey similar dynamics and seasonal patterns while some stand out from the rest as their behavior differs from the expected. The first indication of such similarities is the ratio of rotational over divergent parts of spectral kinetic energy; their seasonality is not as strong as in Western Boundary Currents. Then, although it was not always possible to uniquely determine horizontal transition scales, we confirmed that all our calculated L_t indeed successfully separate mesoscale from submesoscale motions for every region and season. In addition, phase differences at the diurnal period between divergence and vorticity intensities are around 2 to 3.5 hours, in perfect agreement with the transient turbulent thermal wind balance (TTTW) system outlined by Dauhajre and McWilliams (2018).

Figure 1. Regions to be studied within each of the Eastern Boundary Currents: California (North Pacific), Canary (North Atlantic), Perú-Chile (South Pacific), and Benguela (South Atlantic). Each tile in the map represents a quasi-quadrangular region of $\sim 6°$ side.

2 Methodology

2.1 LLC4320 and $\omega - k_h$ spectra

The primary data source is the LLC4320 global ocean simulation output that uses the MITgcm. LLC4320 is a realistic, high-resolution simulation (24-second steps, $1/48°$ horizontal grid spacing, 90 vertical levels with $\mathcal{O}(1m)$ resolution at the top 100 m), and spans 14 months from September 2011 to November 2012, for which hourly snapshots are available. The model is forced with 16 tide constituents and high frequency atmospheric boundary conditions. The interaction between wind and ocean occurs at the ocean surface, where they exchange energy and momentum. Roughly speaking, surface wind stress is commonly parameterized as

$$\tau_s = \rho_{air} C_D \, |U_{wind} - U_{ocean}| \, (U_{wind} - U_{ocean}), \tag{1}$$

where ρ_{air} is the density of the air, C_D is known as the drag coefficient, U_{wind} is the wind speed field, and U_{ocean} is the surface ocean speed (Flexas et al., 2019). On the other hand, ocean net heat flux is parameterized as

$$Q_{net} = Q_{rad} + Q_{lat} + Q_{sen}, \tag{2}$$

where Q_{rad}, Q_{lat}, and Q_{sen} are the radiation, latent, and sensible heat fluxes, respectively (Pinker et al., 2014). As we will see later in this paper, both wind stress and net heat flux modulate mesoscale and submesoscale regimes. Therefore, evaluating the impact of atmospheric forcing on our observed variables is crucial.

Since $1/48°$ horizontal spacing is equivalent to ~ 2 km at mid latitudes, numerical diffusion yields an effective resolution about four times the grid size (~ 8 km) (Rocha et al., 2016; Erickson et al., 2020), LLC4320 allows us to observe and study submesoscale features. In this study, as we aim to compare the dynamics of EBC during the winter (February-February-March) and summer (August-September-October) months, we used hourly snapshots of LLC4320 for these months to examine the vortical features of EBC, resulting in about 2200 snapshots for each variable (e.g., U, V, θ), season and depth. Data can be accessed by either directly downloading it from the ECCO Data Portal (see: `https://data.nas.nasa.gov/ecco/data.php?dir=/eccodata/llc_4320`) or reading it using the xmitgcm Python package (see: `https://github.com/MITgcm/xmitgcm`).

Now, for a given variable $\phi(x, y, t)$ (e.g., kinetic energy, sea surface height), season (summer or winter), region (tiles in Figure 1), and vertical level, by performing a Fast Fourier Transform we get its 3D spectral density in the wavenumber (k, l) and frequency (ω) domains, $\Phi(k, l, \omega)$. A close examination of $\Phi(k, l, \omega)$ on the k-l plane confirms that they are mostly azimuthally symmetric for all frequencies, so that we can map the k-l plane into a horizontal wavenumber $k_h = \sqrt{k^2 + l^2}$; hence the azimuthally averaged spectrum $\Phi(k_h, \omega)$ results.

An example of these isotropized spectra is shown in Figure 2, which also displays reference temporal and spatial scales; an approximate calculation of the local buoyancy frequency N is used to plot dispersion relation curves corresponding to the first four and the tenth vertical modes of IGW. Also, frequency bands at periods of 1 day and 12 hours are present for horizontal scales below 100 km, which exhibit tidal forcing and thus internal tides at those frequencies.

Figure 2. Power spectral density of surface relative vorticity (RV) in frequency-horizontal wavenumber (ω–k_h) domain for the region centered at 16.4°N within the Canary current during winter (January-February-March) 2012. The black dotted lines represent dispersion relations for modes 1, 2, 3, and 10 of internal gravity waves. The black dashed line denotes the minimum frequency between IGW mode 10 and the M_2 tide. The solid dark pink line corresponds to the average Coriolis frequency at that region.

Figure 3. Spectral density in the horizontal wavenumber domain for the region centered at 16.4°N within the Canary current during winter (January-February-March) 2012. The total kinetic energy spectrum (blue dashed) is the sum of its rotational (green solid) and divergent (orange solid) parts. The red vertical line shows the transition scale (L_t = 66.59 km), where both ζ and δ parts equal.

2.2 Filtering submesoscale motions

Once obtained, integration of these $\omega - k_h$ spectra for all frequencies yields wavenumber-domain spectra. If we apply it to the divergent and vortical components of the kinetic energy (via Helmholtz decomposition), we can determine at which horizontal spatial scales the motion is dominated by either divergence or rotational motions. Generally, one might expect rotational (e.g., geostrophic) motions to dominate at large scales, whereas divergent motions (IGW mostly) are predominant at smaller scales. Thus, there should be a spatial scale where both motions equally contribute to the kinetic energy (see, e.g., Fig. 3). Such scale is the so-called *transition scale* (L_t) and is interpreted as the scale at which the variance of the balanced motions is equal to the variance of unbalanced motions (Qiu et al., 2018). Hereinafter, we will label motions larger than L_t as "mesoscale", and the smaller ones as "submesoscale", without quotation marks.

Given the calculation of L_t for each region, we use this scale as the cutoff horizontal wavenumber k_h for a spatial 2D filtering on the horizontal velocities. Submesoscale correspond to the high-pass filtered fields while mesoscales correspond to the low-pass filtered motions. This definition of submesoscale varies from region to region and allows us to characterize those regions physically. The following steps will study one or both *scale ranges*.

2.3 Spatial variability of vorticity and divergence fields

This work analyses the standard deviation of normalized vorticity (ζ/f) and divergence (δ/f) fields in the submesoscale regime, where f is the local Coriolis parameter. Since both divergence ($\delta = u_x + v_y$) and vorticity ($\zeta = v_x - u_y$) have almost zero spatial mean in the ocean (Shcherbina et al., 2013), its standard deviation can be approximated by

$\sigma[S](t) \simeq \sqrt{(NM)^{-1} \sum_{n=0,m=0}^{N,M} \left(S_{n,m}(t)\right)^2} = RMS[S](t)$, thus serving as a measure of the instantaneous average intensity of these fields. If one calculates the standard deviation of these variables for each hourly snapshot, we obtain a time series that shows the evolution of such fields's intensity.

2.3.1 Coherence and phase difference between average intensities of divergence and vorticity

Close inspection of both time series shows a temporal phase shift between them for the diurnal frequency component. As this shift might not be evident for time series with several frequency components, we calculated cross power spectral density $P_{\zeta\delta}(\omega)$ (Welch, 1967), from which we obtained phase differences between both signals as a function of frequency; a positive shift implies that δ precedes ζ, and conversely. We then used Welch's method to obtain spectral coherence between δ and ζ, $C_{\zeta\delta}(\omega)$, in the form

Figure 4. The quotient of spectral densities KE_ζ / KE_δ in the frequency-horizontal wavenumber domain for the selected regions by current and season at selected regions within California (26.64°N: a and b), Canary (26.64°N: c and d), Peru (21.61°S: e and f), and Benguela (26.64°S: g and h) current systems. Green and orange highlight scales where either KE_ζ or KE_δ dominate, respectively. The red vertical line shows the horizontal transition scale (L_t).

$$C_{\zeta\delta}(\omega) = \frac{\left|P_{\zeta\delta}(\omega)\right|^2}{P_{\zeta\zeta}(\omega)\, P_{\delta\delta}(\omega)}, \tag{3}$$

where $P_{AB}(\omega) = |P_{AB}(\omega)|\, e^{i\theta(\omega)}$ is the cross spectral density between variables A and B. Spectral coherence is the frequency-domain analogue of the correlation coefficient (Biltoft & Pardyjak, 2009) so that values near 1 indicate high correlation at a given frequency or, in other terms, that such frequency contributes mainly to the total covariance. This methodology allowed us to confirm that diurnal divergence drives submesoscale vorticity in winter, but this result does not hold on summer.

3 Results

This section will show most of our results and comparisons for regions centered at the same latitude whenever possible. We compare regions at 26.64° (north or south) for the California, Canary, and Benguela currents, and at 21.61°S for the Peru current. Despite this choice, we will later show that our results and conclusions hold for all regions and seasons, except when we state otherwise.

3.1 $\omega - k_h$ spectra

We first calculated the corresponding $\omega - k_h$ kinetic energy spectra densities $KE_\zeta = \left|\hat{\zeta}\right|^2 / k_h^2$ and $KE_\delta = \left|\hat{\delta}\right|^2 / k_h^2$, where $\hat{\zeta}$ and $\hat{\delta}$ denote the Fourier transform of relative vorticity and divergence fields, and $k_h = \sqrt{k_x^2 + k_y^2}$ is the horizontal wavenumber. Figure 4 shows how the quotient of spectral densities KE_ζ / KE_δ varies by current and season, making it evident that vorticity fields dominate on a broader range of frequencies in winter than they do in summer.

From these spectra, we can find out at which temporal and spatial scales each motion dominates. Concerning time scales, at periods of 1 day, both divergence and vorticity have roughly the same energy; kinetic energy for motions above that frequency band is explained mainly by its divergent component (internal waves, mostly), and below that frequency, it is the vortical part (balanced motions) that takes most of the energy. In contrast to their western counterparts (see Torres et al. (2018), Fig. 6), the region in the $\omega - k_h$ spectra that separates both regimes in EBC does not vary substantially between seasons. Lastly, the transition scales shown in the figure are almost identical, except for the California current; we observed the same behavior when we compared *Lt* for a region in the California current and another one at a similar latitude.

3.2 Transition scale from mesoscale to submesoscale and filtered motions

We should also bear in mind that although submesoscales are typically defined below a fixed horizontal scale (e.g. 10 km or 5 km), no rule is suitable for all cases, so we must invoke more dynamical criteria to find these transition scales. This situation becomes significantly more challenging on EBC, where we have shown that vortical and divergent contributions to the kinetic energy are roughly of the same order. Table 1 shows the transition scales for all regions and seasons, calculated as described in 2.2. First, we note that in all cases, ex-

Current	Latitude	Summer L_t [km]	Winter L_t [km]
California	48.4°N	97.52	40
California	44.5°N	118.7	44.5
California	40.4°N	172.16	37.18
California	36.05°N	94.29	41.19
California	31.46°N	107.77	32
California	**26.64°N**	**115.97**	**32**
Canary	31.46°N	70.06	60
Canary	**26.64°N**	**73.42**	**60**
Canary	21.61°N	77.7	61
Canary	16.40°N	129.32	66.59
Peru	16.39°S	76.48	63.94
Peru	**21.61°S**	**74.28**	**61.88**
Peru	40.41°S	66.23	76
Benguela	11.03°S	125.72	64.44
Benguela	16.39°S	122.71	64.19
Benguela	**26.64°S**	**119.46**	**61.3**

Table 1. Transition scales L_t (in km) by current, latitude and season. Red indicates scales that could not be uniquely determined. Rows in bold mark the regions we compare through this paper.

cept in southern Peru current, L_t is more significant in summer than in winter. Also, L_t tends to be larger as we approach the Equator, but the trend is not noticeable. These patterns agree with Qiu et al. (2018) even though we used a different approach. However, our method remains to prove its effectiveness in isolating submesoscales.

It is noteworthy that it was unfeasible to determine L_t in winter in about half the cases. When we found more than one intersection of KE_{RV} and KE_{DIV} spectra, we picked the one that shows a higher separation of both spectra for more minor scales, also enforcing spatial continuity of L_t, so transition scales from neighbor regions were considered; when there is no intersection, we took the horizontal scale for which both ζ and δ spectra are the closest.

Another point of dynamical comparison is the ζ-δ joint probability distribution of both divergence and vorticity fields for each season and region. In Fig 5, a snapshot of both fields is displayed for winter and summer seasons, along with their corresponding joint probability distribution functions (joint PDFs, or JPDFs); although each PDF is built for a single point in time, they put in evidence how dynamical differences in physical space can be translated into a PDF that can be interpreted, in turn allowing to describe these dynamical differences for collections of several snapshots (e.g. a given day, month or season). As typically expected, we find a stronger vorticity field in winter (yielding a "horizontal" distribution), whereas divergence (primarily associated with IGW) is more dominant in summer (the distribution is more "vertical"). Also, each of these four quadrants corresponds to different motion regimes; in particular, higher probability densities found in the fourth quadrant (positive RV, negative DIV) and Rossby numbers ζ/f near order 1 give us evidence of intense submesoscale activity. These differences are under the difference in horizontal temperature and density gradients, which are directly associated with submesoscale instabilities such as fronts or filaments.

Figure 6 shows the joint probability distributions at the four selected regions in winter and summer seasons for their corresponding submesoscale ($< L_t$) regime. The first thing we can see is that in agreement with what both wavenumber and frequency-wavenumber spectra showed, horizontal divergence predominates over vorticity in summer while vorticity is more

Figure 5. Snapshots of relative vorticity (RV: a and b), divergence (DIV: c and d), and instantaneous RV-DIV joint probability distributions (e and f) at Canary (26.64 N), for summer (a, c and e) and winter (b, d and f) when sea surface temperature is maximum (around 1700 local time). RV (ζ) and DIV (δ) are high-pass filtered to preserve motions below the transition scale (L_t = 73.4 km in summer, L_t = 60 km in winter), then normalized by the Coriolis frequency f. Joint PDFs colors are presented on a logarithmic scale.

Figure 6. Joint probability distribution of ζ (x axis) and δ (y axis) at selected regions within California (26.64°N: a and b), Canary (26.64°N: c and d), Peru (21.61°S: e and f) and Benguela (26.64°S: g and h) current systems. Both vorticity (ζ) and divergence (δ) are normalized by f. Bin colors are presented on a logarithmic scale.

intense in winter, with Rossby numbers higher than 1. Also, positive skewness on ζ and negative skewness on δ identify frontogenesis events, the fundamental piece of submesoscale motions. Although this behavior is more visible in winter across all EBC, Canary is the current with the highest submesoscale activity in summer. These seasonal differences in skewness are under what Rocha et al. (2016) obtained in the Kuroshio Extension. A direct implication of this result is that the transition scales we just obtained do capture submesoscale motions, even though some values of L_t might appear more significant than generally expected, along with the fact that, in some cases, the transition scale could not be uniquely determined.

3.3 Phase difference between divergence and vorticity in the submesoscale regime

For all regions, we calculated the averaged square intensity (RMS) of surface divergence and vorticity for both mesoscale ($> L_t$) and submesoscale ($< L_t$) motions. Along with these dynamical quantities, we also considered the evolution of average values of their corresponding atmospheric forcing (wind stress and net heat flux), surface temperature, and KPP boundary layer depth (MLD). These calculations were performed for both seasons, with additional 15 or 30 days (when available) to determine whether there are seasonal transitions. Figures 7 and 8 show the time series of such variables for the Canary and Benguela current systems, respectively.

In addition to the well-known seasonal variability in the MLD (deeper in winter and shallower in summer), some factors impact its depth in the high-frequency regime. We note in our time series (Figs. 7 and 8) that strong winds are followed by a deepening of the mixed layer depth, regardless of the season or current system; simultaneously, MLD displays a variability in phase with the diurnal cycle of the ocean net heat flux (red line in the second row). There is also an evident change in pattern at the end of both seasons, primarily visible in the SST (blue line, second row), along with its corresponding submesoscale DIV and RV intensities (fourth row).

Now, if we center our attention on the mesoscale and submesoscale fields (third and fourth rows in Figs. 7 and 8), we can note that lower frequencies account for most of the mesoscale variability in both seasons, and similarly for submesoscales in summer, while high frequencies are the ones that dominate winter submesoscale motions. Also, submesoscale RV and DIV have higher RMS values in winter than in summer. This behavior has been reported previously around the global ocean (Su et al., 2018), also supported by the spatial decomposition described in the previous subsection. During winter, when the MLD reaches its maximum depth (around 250m in Canary Current and 150 m in Benguela Current), high-frequency variability is more intense in winter, such that RMS values of DIV and RV are more significant at diurnal time scales by a factor of ~2, i.e., from 0.3 to 0.5 in vorticity and 0.2 to 0.4 in divergence. From late winter to early spring, their diurnal pattern weakens, even vanishes for a couple days; this dampening is evidenced by a reduction in the amplitude of near-diurnal variability. The rea-

Figure 7. Time series of dynamical variables for the region centered at 26.6°N within the Canary current from August 1 to November 13 2012 (a, c, e, and g) and from January 1 to April 30 2012 (b, d, f, and h) seasons. First row (a and b): mean values of wind stress ($|\tau|$, blue) and mixed layer depth (MLD, red). Second row (c and d): mean values of sea surface temperature (T, blue) and ocean net heat flux (oceQnet, red). Third row (e and f): standard deviation of the mesoscale normalized vorticity (ζ/f, magenta) and divergence (δ/f, green) fields. Fourth row (g and h): standard deviation of the submesoscale normalized vorticity (ζ/f, magenta) and divergence (δ/f, green) fields.

Figure 8. Time series of dynamical variables for the region centered at 26.6°S within the Benguela current from January 1 to April 30 2012 (a, c, e, and g) and from August 1 to November 13 2012 (b, d, f, and h) seasons. First row (a and b): mean values of wind stress ($|\tau|$, blue) and mixed layer depth (MLD, red). Second row (c and d): mean values of sea surface temperature (T, blue) and ocean net heat flux (oceQnet, red). Third row (e and f): standard deviation of the mesoscale normalized vorticity (ζ/f, magenta) and divergence (δ/f, green) fields. Fourth row (g and h): standard deviation of the submesoscale normalized vorticity (ζ/f, magenta) and divergence (δ/f, green) fields.

Figure 9. Evolution of mean values (a and b panels) of wind stress intensity, mixed layer depth, ocean net heat flux and sea surface temperature, compared with RMS values (c and d panels) of mesoscale and submesoscale relative vorticity (ζ, magenta) and divergence (δ, green) fields for the region centered at 26.6°N within the Canary current, spanning from the last week of February and the first week of March 2012. Background color represents day (red) and night (blue) periods. L_t = 60 km. Vertical dashed blue and red lines correspond to March 1 morning (around 0500 local time) and afternoon (around 1700 local time), respectively, marking the times where vorticity and divergence nearly reach their minimum and maximum.

son behind our choice of comparing Canary and Benguela currents lies behind the fact that their RV, DIV and SST maps have less in common, especially in winter: Canary has high temperature (and hence density) gradients and is located near a source of solid eddies that are ejected towards the West Atlantic; Benguela current around 26 S, on the other hand, has a weaker vorticity field and is mainly dominated by internal tides, produced by topographic waves at the Walvis Ridge.

Submesoscale surface fronts are affected by atmospheric forcings at time scales of a few hours (Dauhajre et al., 2017). Figure 9 illustrates the synchronization of divergence RMS with the ocean net heat flux. This figure emphasizes the day and night variation, being maximum when the net heat flux is maximum. However, when the wind stress increases from 0.1 N/m^2 to 0.15 N/m^2, the amplitude of the RMS values of vorticity and divergence decreases. Sun et al. (2020) discussed that an increase in mixing when wind bursts occur reduces the vertical shear that weakens the divergence and vorticity.

By closely inspecting the time series of vorticity and divergence in the submesoscale regime, one can, in most cases, spot there is an apparent delay between changes in the intensity of these two kinematic quantities (Fig. 9, lower panel); this pattern has been observed at all EBC time series at near-diurnal frequencies, particularly in winter. To give a more quantitative perspective, Table 2 shows the different phase differences calculated by season and region for the diurnal (24 h) frequency. The first thing we note is that coherence between DIV and RV is consistently high in winter, with values above 0.95 in most cases, while phase difference shows a slight tendency to higher values (towards 3.5 h) in high latitudes, with lower values (around 2 h) as we get closer to the tropics. These delays match what Dauhajre and McWilliams (2018) found using their transient turbulent thermal wind balance (TTTW) system, which takes into consideration the difference between the maximum (K_{max}) and minimum (K_{min}) RMS val-

Current	Latitude	Summer Δt [h]	Summer $C_{\zeta\delta}$	Winter Δt [h]	Winter $C_{\zeta\delta}$
California	48.4°N	-0.14	0.69	3.31	0.93
California	44.5 °N	10.77	0.15*	3.4	0.95
California	40.4 °N	4.23	0.00*	3.03	0.95
California	36.05 °N	2.34	0.8	2.68	0.95
California	31.46 °N	3.34	0.65*	2.6	0.98
California	**26.64°N**	**1.42**	**0.75***	**2.72**	**0.99**
Canary	31.46°N	2.49	0.75	3.5	0.99
Canary	**26.64°N**	**2.08**	**0.61***	**3.35**	**0.99**
Canary	21.61°N	-1.8	0.29*	2.94	0.99
Canary	16.40°N	-4.12	0.41*	2.32	0.98
Peru	16.39°S	-7.85	0.29*	2.69	0.99
Peru	**21.61°S**	**-10.47**	**0.03***	**3**	**0.99**
Peru	40.41°S	0.46	0.56	2.12	0.96
Benguela	11.03°S	-6.4	0.29*	0.73	0.77
Benguela	16.39°S	-8.67	0.54	2.01	0.75
Benguela	**26.64°S**	**-6**	**0.49***	**2.72**	**0.98**

Table 2. Phase difference Δt (in hours) between normalized divergence (δ) and vorticity (ζ) by current, latitude, and season. The phase difference is the angle of the complex power spectral density, calculates with a window of 10 days. All phase differences shown correspond to the diurnal (24 h) cycle. Positive values indicate that divergence occurs first and is then *followed* by relative vorticity. Rows in bold mark the regions we compare through this paper. Values with an asterisk (*) correspond to the case when their coherence did not pass the F-test for 90% confidence interval.

ues of the vertical viscosity ($\Delta K = K_{max} - K_{min}$), the period at which it varies (T_κ), and the mixed layer depth (H), described in its 1D formulation by the system of non-dimensional equations:

$$\begin{pmatrix} u \\ v \end{pmatrix}_t + \Gamma \begin{pmatrix} -v \\ u \end{pmatrix} - \Gamma \left[\mathcal{K}(t) + k\right] \begin{pmatrix} u \\ v \end{pmatrix}_{zz} = \mathcal{K}(t)\,(1-\Gamma) \begin{pmatrix} \overline{u} \\ \overline{v} \end{pmatrix}, \tag{4}$$

where subscripts indicate partial derivatives, $\overline{\mathbf{u}} = (\overline{u}, \overline{v})$ is the steady solution, $\mathcal{K}(t) = \cos 2\pi T_\kappa$, $k = 2K_0/\Delta K$ and $\Gamma = T\Delta K/2H^2$; this 1D Ekman layer dynamics is highly determined by atmospheric forcings, as well as by their impact on the amplitude (ΔK) and frequency (or period T_κ) of the variability of the vertical viscosity. In summer, the calculated coherence is not statistically significant, consistent with the weak diurnal cycle signature in Figures 7 and 8 (fourth row in left panel).

Maps of vorticity and divergence are visualized in Figure 10, where snapshots at approximately the daily maximum and minimum and when the wind stress is minimum. In most cases in all EBC, the maximum in divergence occurs around 1700 local tine, and the minimum around 0500 (local times), with the only differences being the intensity of these fields and the time where their minima a maxima occur. Submesoscale structures strongly emerge during the afternoon with positive skewness on vorticity (Rossby number > 1) and negative skewness on divergence. Towards 0500, the vorticity and divergence decrease, therefore the skewness indicates that frontogenesis is much more significant during the afternoon than at night. Since upward vertical heat fluxes in the ocean are driven by submesoscale frontogenesis, the results

Figure 10. Snapshots of relative vorticity (ζ: a and b), divergence (δ: c and d), and instantaneous ζ-δ joint probability distributions (e and f) at Canary (26.64°N), for times where sea surface temperature is maximum (around 1700 local time, left) and minimum (around 0500 local time, right) at an arbitrary day in winter (marked by a vertical dashed lines in Figure 9). Divergence and relative vorticity are high-pass filtered to preserve motions below the transition scale (L_t = 60 km), then normalized by the local Coriolis frequency f. Joint PDF colors are presented on a logarithmic scale.

discussed here suggest that atmospheric forcing at short time scales may affect the restratification process.

4 Discussion

This paper presented an analysis in both physical and spectral spaces of submesoscale divergence and relative vorticity fields in EBC, using the output of a tide-resolving, submesoscale permitting, global ocean simulation (a.k.a LLC4320). It is the first time that submesoscale motions are compared between the four major EBC. Our results show that it is still possible to filter submesoscale motions in low kinetic energy currents such as the EBC, where submesoscales are not as intense as they are in other areas of the ocean.

A first conclusion we can make is that EBC remain similar in the submesoscale regime, despite having differences in their density profiles or topographic features. The only exception was found at the Peru current around 40°S where, unlike the rest of the regions we analyzed, we found a larger transition scale L_t in winter that in summer, so our results for this region could not be entirely consistent with what we found other regions, since motions below L_t (76 km) might be capturing mesoscales as well.

The method we propose to filter submesoscale works reasonably well in most cases within the EBC, in both winter and summer seasons. At this point, we could argue that a more dynamical approach to calculate submesoscale transition scale L_t would be more precise, as proposed by Qiu et al. (2018), who compare the contribution to total kinetic energy for frequencies below and above the highest IGW mode or lowest frequency permissible tides. In contrast, the method presented here compares the divergent and vortical contributions to the total energy, considering all frequencies. Despite the apparent differences in these two ways of isolating submesoscale motions, they are equivalent to some extent since, as shown in Figure 4, divergence is more energetic than vorticity within the region in the $\omega - k_h$ space, like what the dynamical filtering would tag as *unbalanced motions*, whereas vorticity would explain most of the *balanced motions*. In addition, our methodology does not require us to know anything about the region of interest, such as the highest IGW mode or its maximum tide frequency; it also does not need any temporal information, as L_t can be found from spectra in the horizontal wavenumber space, as shown by Figure 3.

Submesoscale motions in EBC emerge primarily from the advective stirring of buoyancy anomalies by mesoscale eddies, which lead to the creation of fronts (frontogenesis) and instabilities such as mixed-layer instabilities. We showed that the increase of RMS values in vorticity and divergence when the mixed-layer depth is more profound. The scenario is consistent with previous studies that reported the intensification of submesoscale activity in winter (Mensa et al., 2013; Callies et al., 2015; Rocha et al., 2016; Su et al., 2018). Once the submesoscale motions populate the upper ocean layer, in the shape of fronts and filaments, they are modulated by heat fluxes that induce diurnal fluctuations on the mixed layer depth, potentially correlated to the vertical viscosity coefficient (κ_ν), as described by Dauhajre and McWilliams (2018). In addition, we confirmed a 2 to 3.5-hour lag between vorticity and divergence fields in winter, with a latitudinal dependency (Fig. 11), as found by the transient turbulent thermal wind (TTTW) system (Dauhajre & McWilliams, 2018). It is worth mentioning that the res-

Figure 11. Lag between divergence and vorticity fields for the four EBC in winter, as a function of the latitude (absolute value). Data points were taken from Table 2, and solid lines correspond to a first-order linear regression, by each current.

olution of LLC4320 is not sufficient to resolve submesoscale instabilities like symmetric instabilities and gravitational instabilities fully. Hence, this implies that in simulations at higher resolution, submesoscale motions are stronger (Sun et al., 2020). This result implies that the diurnal cycle reported here is underestimated. However, the general picture of the diurnal cycle agrees with the theoretical description of Dauhajre and McWilliams (2018): the maximum of divergence at mid-afternoon, followed by a maximum in vorticity with 2 to 3 hour lag, in turn, forced by variations in net ocean heat flux and wind stress, parameterized by Equations 2 and 1 respectively.

However, we did not find any clear evidence of this RV-DIV lag at diurnal cycles in summer within any of the EBC regions we studied here. A straightforward explanation would rely on the lack of submesoscale features in summer, such as high horizontal temperature gradients, weaker winds (hence less mixing processes occur), and an increased heat flux that increases stratification and consequently makes the mixed layer shallower. However, after a closer look into the time series in Figs. 7 and 8, we can see there is some variability at semidiurnal and quarter-diurnal frequencies involved, but with a much lower amplitude. Hence, it could also be possible that the period at which vertical turbulent viscosity coefficient (κ_v) changes is lower (potentially around 12 and 6 hours), but the variation (ΔK in Eq. 4) is not that notable, perhaps because the range at which MLD varies during each day is not as high in summer as in winter. This result leads us to the hypothesis that MLD and κ_v could be tightly linked, even directly proportional, at least at first order in winter. A more in-depth analysis of these higher-frequency variabilities in the κ_v coefficient needs to be made in future research in order to validate the latter hypothesis, also whether TTTW system still holds for the cases when submesoscales are not that active.

5 Conclusions

This work contributes to understand the Eastern Boundary Currents in the submesoscale regime, first by being able to isolate submesoscale motions by a given horizontal transition scale, L_t, using an alternative, potentially more practical method; then by identifying the air-sea coupling factors that have the most impact on them, namely diurnal changes in the eddy viscosity induced by wind stress and ocean heat fluxes.

The results found in the present study are of interest since it has been found that the diurnal cycle of submesoscale motions is more robust in winter than in summers. This scenario might be considered at the design and interpretation phases of upcoming experiments, such as the S-MODE (Sub-Mesoscale Ocean Dynamics Experiment) that will take place close to the coast in the central part of the California Current System during the spring and fall seasons, or the SWOT Cal/Val (calibration and validation) in situ campaign that will also occur in the central part of the California Current System. The in situ observations from the SWOT CalVal will be used in combination with sea surface height at high spatial and temporal (daily) resolution provided by the SWOT mission during the Fast Sampling Period. Such combination will be a unique opportunity to study submesoscale motions in the EBC, before being properly discriminated. The method described here can applied to that end by invoking the transition scale, L_t.

Acknowledgments

This research was supported by Centro de Investigación Científica y de Educación Superior de Ensenada (CICESE). The first author receives a grant from Consejo Nacional de Ciencia y Tecnología (CONACyT).

Data availability statement

The LLC4320 model data output used in this study are available at as binary files at the ECCO Data Portal (`https://data.nas.nasa.gov/ecco/data.php?dir=/eccodata/llc_4320`). Version 0.5.1 of the xmitgcm package used for reading LLC4320 data files from ECCO Data Portal is preserved at `https://doi.org/10.5281/zenodo.4574204` via `https://github.com/MITgcm/xmitgcm` (Abernathey et al., 2021). Version 1.1.0 of the code we developed to perform further analyses (e.g. calculation of time series or frequency-wavenumber spectra of physical variables) is preserved at `https://doi.org/10.5281/zenodo.5117940` via `https://github.com/antonimmo/ocean-wk-spectral-analysis` (Quintana, 2021).

References

Abernathey, R., Dussin, R., Smith, T., Fenty, I., Bourgault, P., Bot, S., ... Brannigan, L. (2021). *Mitgcm/xmitgcm: v0.5.1*. Zenodo. doi: 10.5281/zenodo.4574204

Biltoft, C. A., & Pardyjak, E. R. (2009). Spectral coherence and the statistical significance of turbulent flux computations. *Journal of Atmospheric and Oceanic Technology*, *26*(2), 403–410. doi: 10.1175/2008JTECHA1141.1

Callies, J., Ferrari, R., Klymak, J. M., & Gula, J. (2015). Seasonality in submesoscale turbulence. *Nature Communications*, *6*(1), 6862. doi: 10.1038/ncomms7862

Chereskin, T. K., & Price, J. F. (2008). Ekman transport and pumping. In *Encyclopedia of ocean sciences: Second edition* (pp. 222–227). Academic Press. doi: 10.1016/B978-012374473-9.00155-7

Dauhajre, D. P., & McWilliams, J. C. (2018). Diurnal evolution of submesoscale front and filament circulations. *Journal of Physical Oceanography*, *48*, 2343-2361. doi: 10.1175/JPO-D-18-0143.1

Dauhajre, D. P., McWilliams, J. C., Uchiyama, Y., Dauhajre, D. P., McWilliams, J. C., & Uchiyama, Y. (2017). Submesoscale coherent structures on the continental shelf. *Journal of Physical Oceanography*, *47*(12), 2949–2976. doi: 10.1175/JPO-D-16-0270.1

Erickson, Z. K., Thompson, A. F., Callies, J., Yu, X., Garabato, A. N., & Klein, P. (2020). The vertical structure of open-ocean submesoscale variability during a full seasonal cycle. *Journal of Physical Oceanography*, *50*(1), 145–160. doi: 10.1175/JPO-D-19-0030.1

Flexas, M. M., Thompson, A. F., Torres, H. S., Klein, P., Farrar, J. T., Zhang, H., & Menemenlis, D. (2019). Global estimates of the energy transfer from the wind to the ocean, with emphasis on near-inertial oscillations. *Journal of Geophysical Research: Oceans*, *124*(8), 5723–5746. doi: 10.1029/2018jc014453

Fréon, P., Barange, M., & Arístegui, J. (2009). Eastern boundary upwelling ecosystems: Integrative and comparative approaches. *Progress in Oceanography*, *83*(1-4), 1–14. doi: 10.1016/j.pocean.2009.08.001

Hill, A. E., Hickey, B. M., Shillington, F. A., Strub, P. T., Brink, K. H., Barton, E. D., & Thomas, A. C. (1998). Eastern Ocean Boundaries, Coastal Segment (E). In A. R. Robinson & K. H. Brink (Eds.), *The sea: The global coastal ocean: Regional studies and syntheses* (Vol. 11, pp. 29–67). Boston, MA: Harvard University Press.

Klein, P., Lapeyre, G., Siegelman, L., Qiu, B., Fu, L. L., Torres, H., ... Le Gentil, S. (2019). Ocean-scale interactions from space. *Earth and Space Science*, 2018EA000492. doi: 10.1029/2018EA000492

Mensa, J. A., Garraffo, Z., Griffa, A., Özgökmen, T. M., Haza, A., & Veneziani, M. (2013). Seasonality of the submesoscale dynamics in the Gulf Stream region. *Ocean Dynamics*, *63*(8), 923–941. doi: 10.1007/s10236-013-0633-1

Müller, M., Arbic, B. K., Richman, J. G., Shriver, J. F., Kunze, E. L., Scott, R. B., ... Zamudio, L. (2015). Toward an internal gravity wave spectrum in global ocean models. *Geophysical Research Letters*, *42*(9), 3474-3481. doi: 10.1002/2015GL063365

Pinker, R. T., Bentamy, A., Katsaros, K. B., Ma, Y., & Li, C. (2014). Estimates of net heat fluxes over the atlantic ocean. *Journal of Geophysical Research: Oceans*, *119*(1), 410-427. doi: 10.1002/2013JC009386

Qiu, B., Chen, S., Klein, P., Wang, J., Torres, H., Fu, L.-L., ... Menemenlis, D. (2018). Seasonality in transition scale from balanced to unbalanced motions in the world ocean. *Journal of Physical Oceanography*, *48*(3), 591–605. doi: 10.1175/JPO-D-17-0169.1

Qiu, B., Nakano, T., Chen, S., & Klein, P. (2017). Submesoscale transition from geostrophic flows to internal waves in the northwestern Pacific upper ocean. *Nature Communications*, *8*(1), 14055. doi: 10.1038/ncomms14055

Quintana, A. (2021). *antonimmo/ebc-wk-spectral-analysis: v1.1.0.* Zenodo. doi: 10.5281/zenodo.5117940

Rocha, C. B., Gille, S. T., Chereskin, T. K., & Menemenlis, D. (2016). Seasonality of submesoscale dynamics in the Kuroshio extension. *Geophysical Research Letters*, *43*(21), 11,304–11,311. doi: 10.1002/2016GL071349

Samelson, R. M. (2017). Time-dependent linear theory for the generation of poleward undercurrents on eastern boundaries. *Journal of Physical Oceanography*, *47*(12), 3037–3059. doi: 10.1175/jpo-d-17-0077.1

Shcherbina, A. Y., D'Asaro, E. A., Lee, C. M., Klymak, J. M., Molemaker, M. J., & McWilliams, J. C. (2013). Statistics of vertical vorticity, divergence, and strain in a developed submesoscale turbulence field. *Geophysical Research Letters*, *40*(17), 4706–4711. doi: 10.1002/grl.50919

Su, Z., Wang, J., Klein, P., Thompson, A. F., & Menemenlis, D. (2018). Ocean submesoscales as a key component of the global heat budget. *Nature Communications*, *9*(1), 775. doi: 10.1038/s41467-018-02983-w

Sun, D., Bracco, A., Barkan, R., Berta, M., Dauhajre, D., Molemaker, M. J., ... McWilliams, J. C. (2020). Diurnal cycling of submesoscale dynamics: Lagrangian implications in drifter observations and model simulations of the northern Gulf of Mexico. *Journal of Physical Oceanography*, *50*(6), 1605–1623. doi: 10.1175/JPO-D-19-0241.1

Thomas, L. N. (2017). On the modifications of near-inertial waves at fronts: Implications for energy transfer across scales. *Ocean Dynamics*, *67*(10), 1335–1350. doi: 10.1007/s10236-017-1088-6

Thomas, L. N., & Ferrari, R. (2008). Friction, frontogenesis, and the stratification of the surface mixed layer. *Journal of Physical Oceanography*, *38*(11), 2501–2518. doi: 10.1175/2008JPO3797.1

Tomczak, M. (1981). Coastal upwelling systems and eastern boundary currents: A review of terminology. *Geoforum*, *12*(2), 179–191. doi: 10.1016/0016-7185(81)90019-1

Torres, H. S., Klein, P., Menemenlis, D., Qiu, B., Su, Z., Wang, J., ... Fu, L.-L. (2018). Partitioning ocean motions into balanced motions and internal gravity waves: A modeling study in anticipation of future space missions. *Journal of Geophysical Research: Oceans*, *123*(11), 8084–8105. doi: 10.1029/2018JC014438

Wang, J., Fu, L.-L., Torres, H. S., Chen, S., Qiu, B., & Menemenlis, D. (2019). On the spatial scales to be resolved by the surface water and ocean topography Ka-band radar interferometer. *Journal of Atmospheric and Oceanic Technology*, *36*(1), 87-99. doi: 10.1175/JTECH-D-18-0119.1

Welch, P. D. (1967). The use of fast Fourier transform for the estimation of power spectra: A method based on time averaging over short, modified periodograms. *IEEE Transactions on Audio and Electroacoustics*, *15*(2), 70–73. doi: 10.1109/TAU.1967.1161901

Figure.

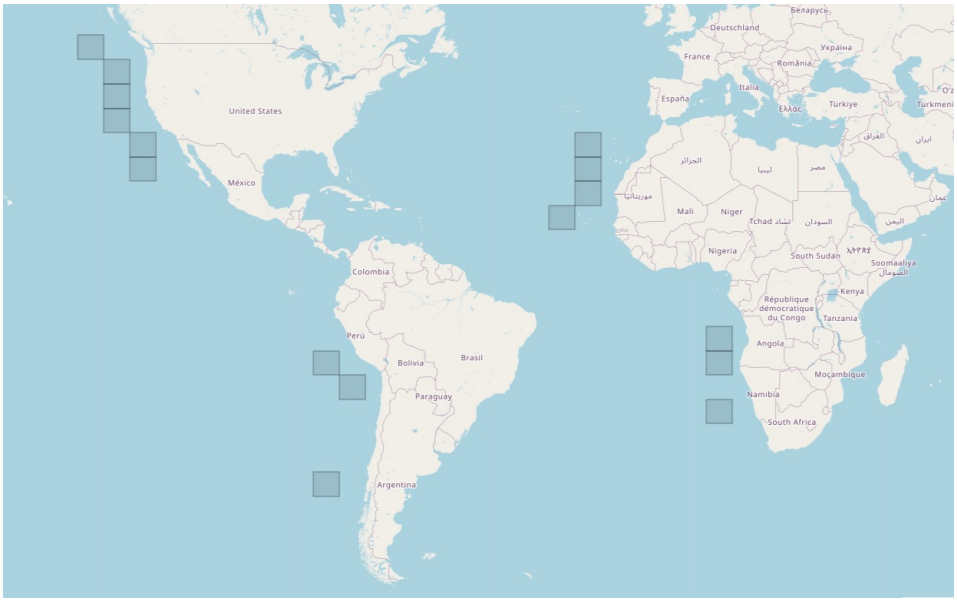

Figure 1. Regions to be studied within each of the Eastern Boundary Currents: California (North Pacific), Canary (North Atlantic), Perú-Chile (South Pacific), and Benguela (South Atlantic). Each tile in the map represents a quasi-quadrangular region of ~ 6° side.

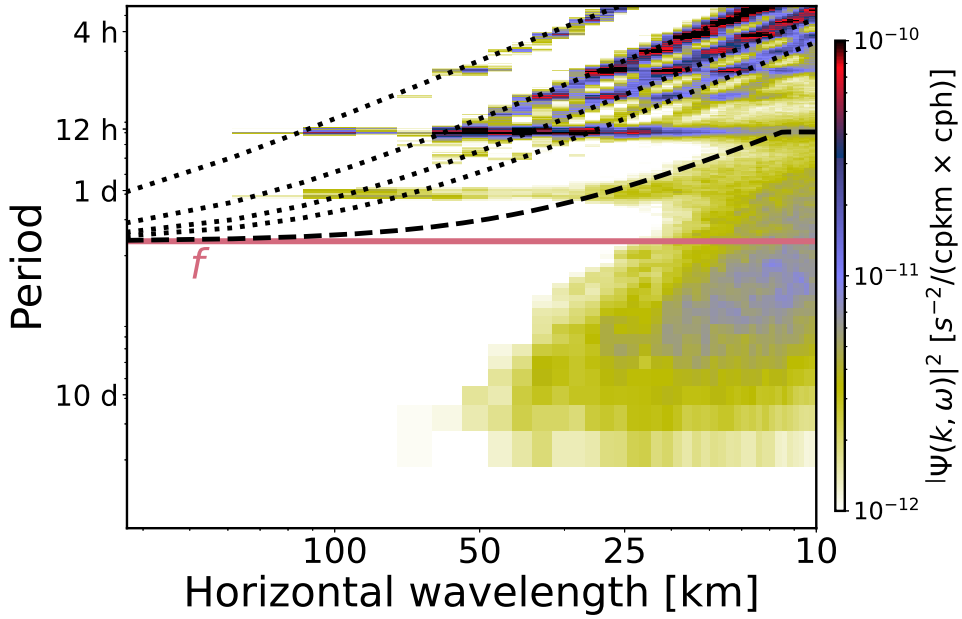

Figure 2. Power spectral density of surface relative vorticity (RV) in frequency-horizontal wavenumber (ω–k_h) domain for the region centered at 16.4°N within the Canary current during winter (January-February-March) 2012. The black dotted lines represent dispersion relations for modes 1, 2, 3, and 10 of internal gravity waves. The black dashed line denotes the minimum frequency between IGW mode 10 and the M_2 tide. The solid dark pink line corresponds to the average Coriolis frequency at that region.

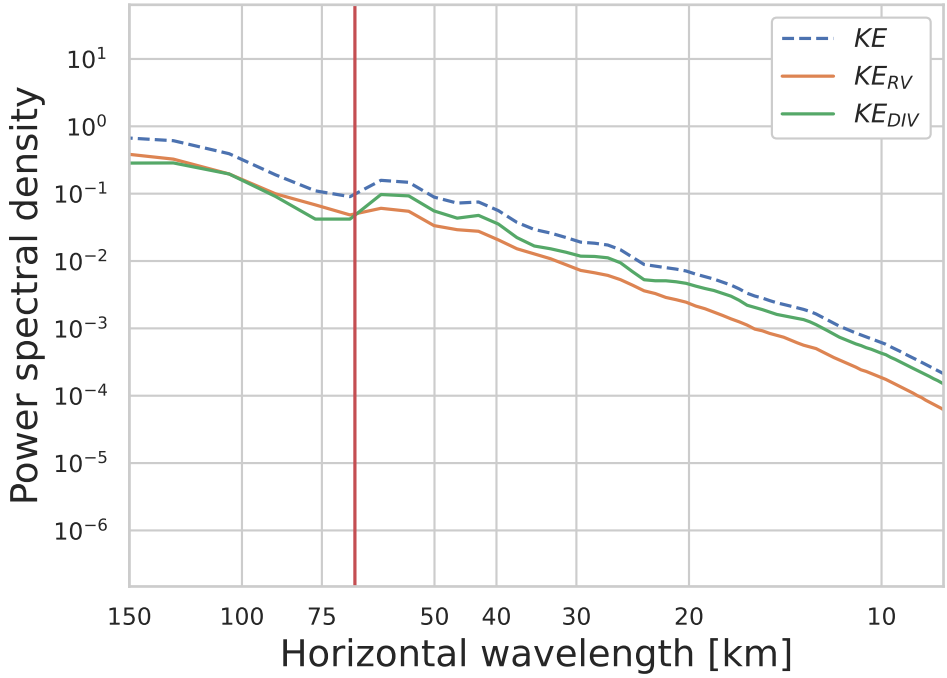

Figure 3. Spectral density in the horizontal wavenumber domain for the region centered at 16.4°N within the Canary current during winter (January-February-March) 2012. The total kinetic energy spectrum (blue dashed) is the sum of its rotational (green solid) and divergent (orange solid) parts. The red vertical line shows the transition scale (L_t = 66.59 km), where both ζ and δ parts equal.

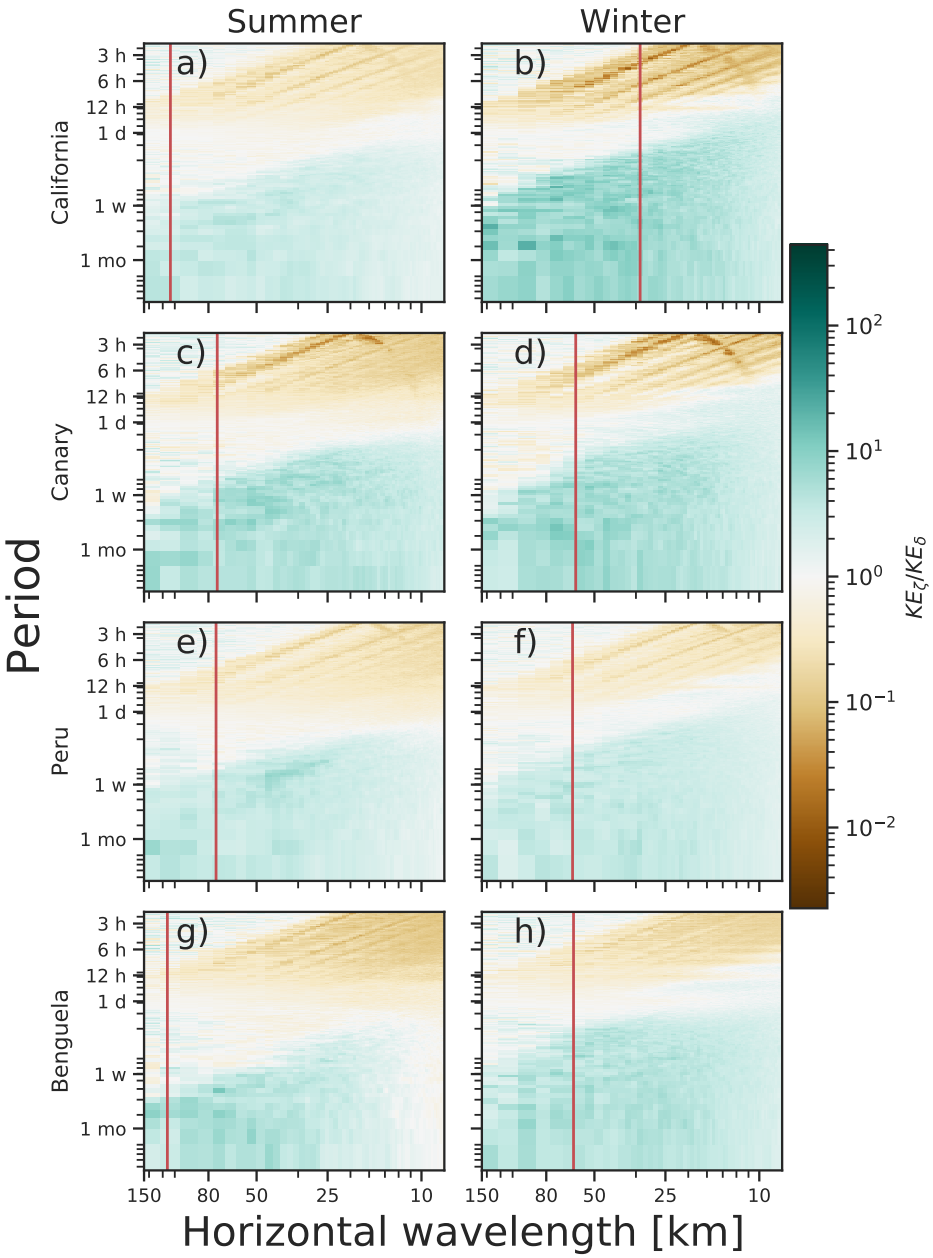

Figure 4. The quotient of spectral densities KE_ζ/KE_δ in the frequency-horizontal wavenumber domain for the selected regions by current and season at selected regions within California (26.64°N: a and b), Canary (26.64°N: c and d), Peru (21.61°S: e and f), and Benguela (26.64°S: g and h) current systems. Green and orange highlight scales where either KE_ζ or KE_δ dominate, respectively. The red vertical line shows the horizontal transition scale (L_t).

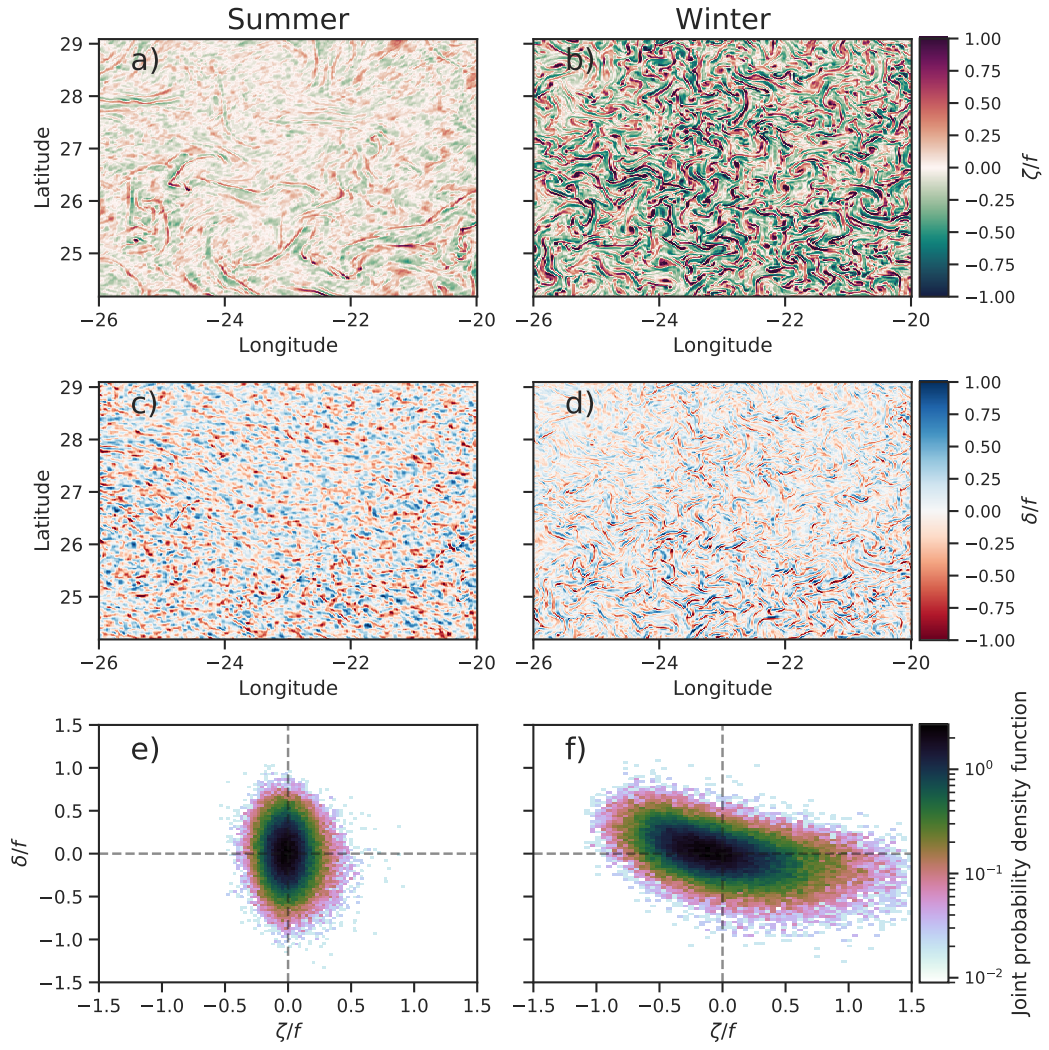

Figure 5. Snapshots of relative vorticity (RV: a and b), divergence (DIV: c and d), and instantaneous RV-DIV joint probability distributions (e and f) at Canary (26.64 N), for summer (a, c and e) and winter (b, d and f) when sea surface temperature is maximum (around 1700 local time). RV (ζ) and DIV (δ) are high-pass filtered to preserve motions below the transition scale (L_t = 73.4 km in summer, L_t = 60 km in winter), then normalized by the Coriolis frequency f. Joint PDFs colors are presented on a logarithmic scale.

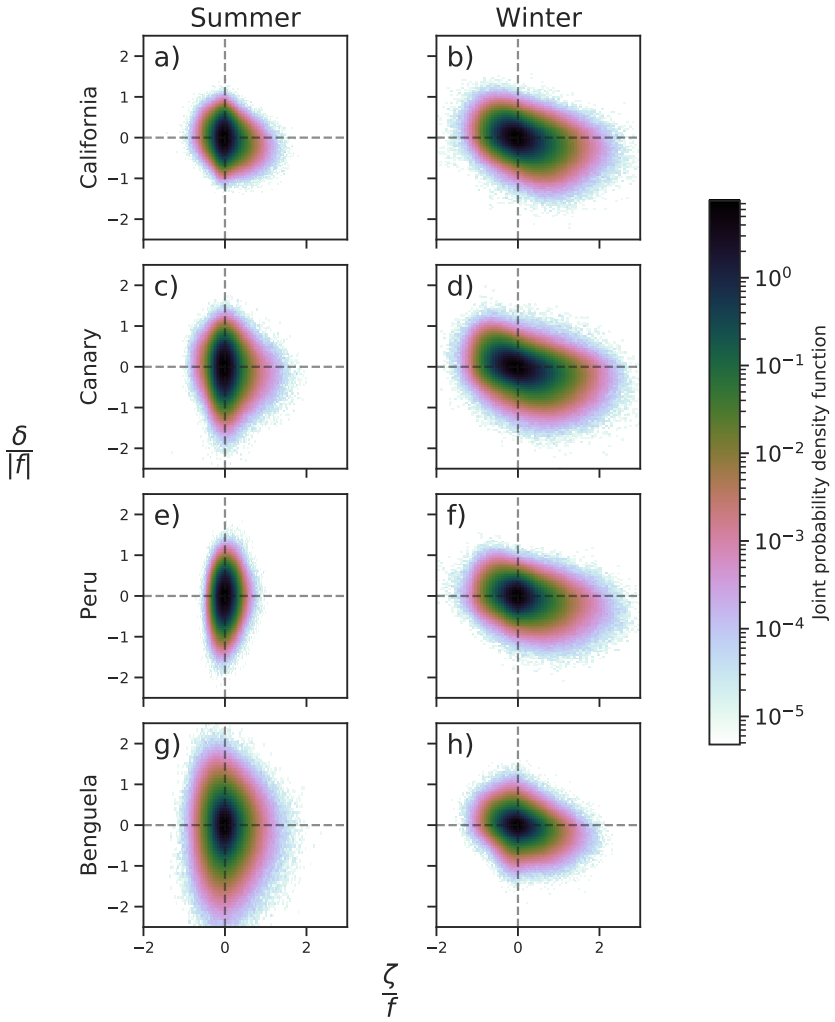

Figure 6. Joint probability distribution of ζ (x axis) and δ (y axis) at selected regions within California (26.64°N: a and b), Canary (26.64°N: c and d), Peru (21.61°S: e and f) and Benguela (26.64°S: g and h) current systems. Both vorticity (ζ) and divergence (δ) are normalized by f. Bin colors are presented on a logarithmic scale.

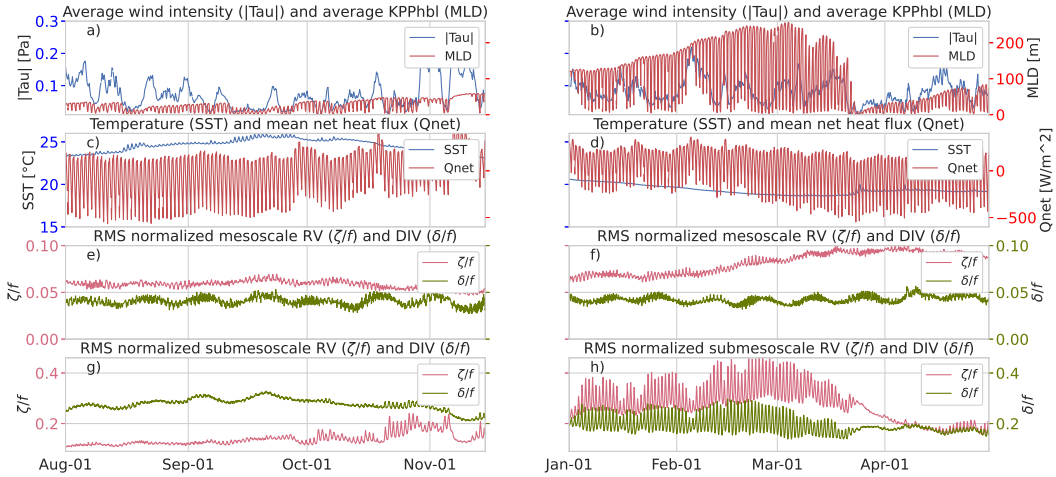

Figure 7. Time series of dynamical variables for the region centered at 26.6°N within the Canary current from August 1 to November 13 2012 (a, c, e, and g) and from January 1 to April 30 2012 (b, d, f, and h) seasons. First row (a and b): mean values of wind stress ($|\tau|$, blue) and mixed layer depth (MLD, red). Second row (c and d): mean values of sea surface temperature (T, blue) and ocean net heat flux (oceQnet, red). Third row (e and f): standard deviation of the mesoscale normalized vorticity (ζ/f, magenta) and divergence (δ/f, green) fields. Fourth row (g and h): standard deviation of the submesoscale normalized vorticity (ζ/f, magenta) and divergence (δ/f, green) fields.

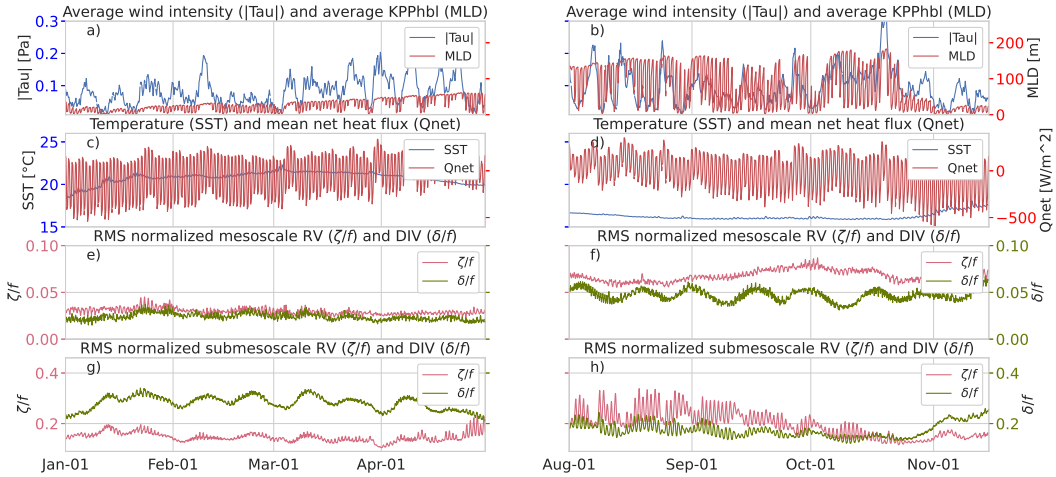

Figure 8. Time series of dynamical variables for the region centered at 26.6°S within the Benguela current from January 1 to April 30 2012 (a, c, e, and g) and from August 1 to November 13 2012 (b, d, f, and h) seasons. First row (a and b): mean values of wind stress ($|\tau|$, blue) and mixed layer depth (MLD, red). Second row (c and d): mean values of sea surface temperature (T, blue) and ocean net heat flux (oceQnet, red). Third row (e and f): standard deviation of the mesoscale normalized vorticity (ζ/f, magenta) and divergence (δ/f, green) fields. Fourth row (g and h): standard deviation of the submesoscale normalized vorticity (ζ/f, magenta) and divergence (δ/f, green) fields.

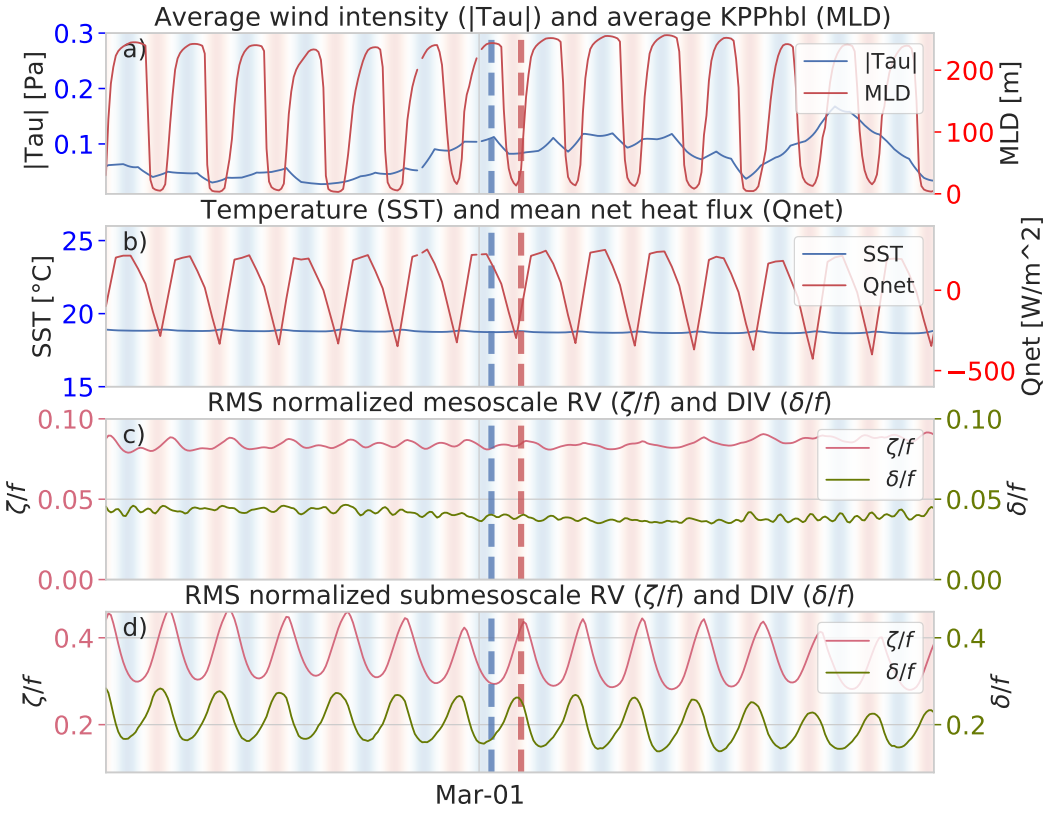

Figure 9. Evolution of mean values (a and b panels) of wind stress intensity, mixed layer depth, ocean net heat flux and sea surface temperature, compared with RMS values (c and d panels) of mesoscale and submesoscale relative vorticity (ζ, magenta) and divergence (δ, green) fields for the region centered at 26.6°N within the Canary current, spanning from the last week of February and the first week of March 2012. Background color represents day (red) and night (blue) periods. L_t = 60 km. Vertical dashed blue and red lines correspond to March 1 morning (around 0500 local time) and afternoon (around 1700 local time), respectively, marking the times where vorticity and divergence nearly reach their minimum and maximum.

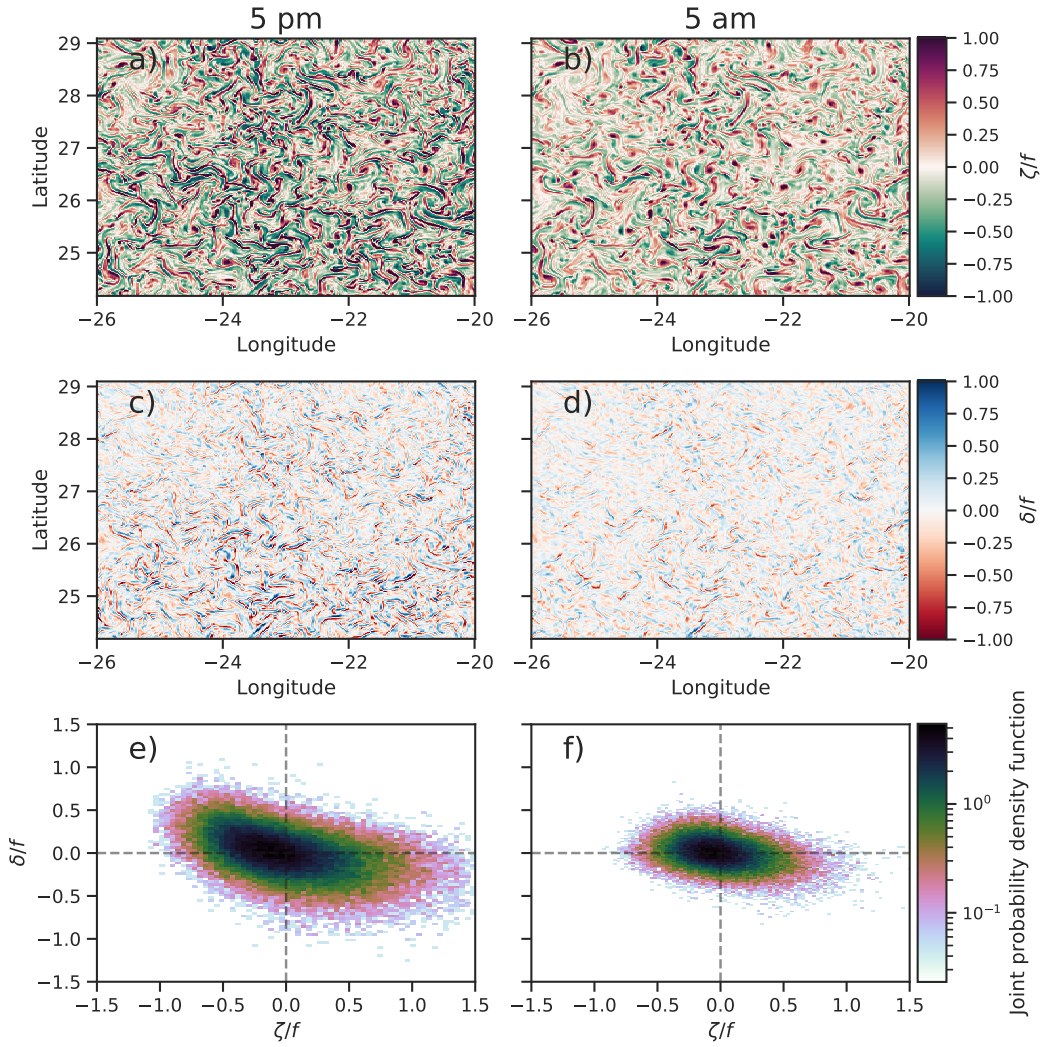

Figure 10. Snapshots of relative vorticity (ζ: a and b), divergence (δ: c and d), and instantaneous ζ-δ joint probability distributions (e and f) at Canary (26.64°N), for times where sea surface temperature is maximum (around 1700 local time, left) and minimum (around 0500 local time, right) at an arbitrary day in winter (marked by a vertical dashed lines in Figure 9). Divergence and relative vorticity are high-pass filtered to preserve motions below the transition scale (L_t = 60 km), then normalized by the local Coriolis frequency f. Joint PDF colors are presented on a logarithmic scale.

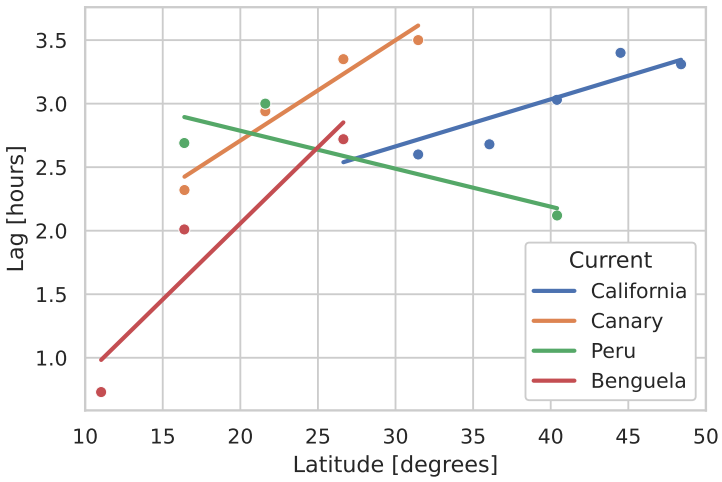

Figure 11. Lag between divergence and vorticity fields for the four EBC in winter, as a function of the latitude (absolute value). Data points were taken from Table 2, and solid lines correspond to a first-order linear regression, by each current.